



# Iron nucleation mechanisms on vitreous carbon during electrodeposition from sulfate and chloride solutions

Darko Grujicic, Batric Pesic \*

University of Idaho, College of Engineering, Department of Materials Science and Engineering, McClure Hall, Moscow, ID 83844-3024, USA

Received 14 September 2004; received in revised form 26 December 2004; accepted 4 February 2005

Available online 17 March 2005

## Abstract

Iron nucleation mechanisms from aqueous solutions onto vitreous carbon electrode were comparatively investigated in iron sulfate and iron chloride systems by utilizing the electrochemical techniques of cyclic voltammetry (cv) and chronoamperometry (ca), coupled with atomic force microscopy (AFM) studies. The investigated parameters were pH, scanning rate, iron concentration, deposition potential and temperature. It was found that iron nuclei population density decreased with increase of pH. On the other hand, the population density increased with increase of iron concentration and cathodic deposition potential. Increase of solution temperature resulted in the increase of nuclei population density in the sulfate system, while the dependence of nuclei population density on temperature in the chloride system was more complex. The experimental electrochemical data fitted the theoretical model describing progressive nucleation mechanisms, which was also confirmed by the AFM morphological studies. In addition, the atomic force microscopy was successful in determining the possible crystallographic orientations of electrodeposited iron nuclei.

© 2005 Elsevier Ltd. All rights reserved.

**Keywords:** Iron nucleation; Vitreous carbon electrode; Sulfate; Chloride; Cyclic voltammetry; Chronoamperometry; Atomic force microscopy (AFM)

## 1. Introduction

Electrodeposition is a viable method for fabrication of thin metallic films [1], the properties of which are of essential importance to the electronic storage industry. Successful development of thin film materials requires the understanding of their earliest stage of formation, i.e. the nucleation, as the initial size and distribution of metal nuclei will determine the physical properties of the final films.

Electrodeposition of pure iron as a ferromagnetic thin film component has received only limited attention, contrary to the well-studied area of electrodeposition of iron alloys [2–6], being among the earliest references. Further, Gow and Hutton [7] have investigated electrodeposition of thick (~25 µm) iron films from sulfate solutions on brass substrates. They found that preferred growth direction was vertical, resulting in columnar deposit structure. Heusler

and Knoedler [8] have investigated the morphology of iron crystal surfaces electrodeposited on platinum substrates, and found that the increase of deposition overvoltage changes the morphology of iron crystals from tetragonal to trigonal pyramids. More recently, Yoshimura et al. [9] have investigated the crystallography of iron films deposited from chloride solutions onto a copper electrode, while Schindler et al. [10] have investigated the magnetic properties of thin iron films electrodeposited on copper electrodes from sulfate solutions. The optimized parameters for iron electrodeposition on copper from electrolytes containing gluconate were reported by Abd El Meguid et al. [11], and boric acid electrolytes by Yin and Lin [12]. Several recent studies of iron electrodeposition by Jartych et al. [13–15], were concerned with the effect of temperature and solution pH on the surface roughness and magnetic properties of thin iron films deposited on an evaporated copper seed layer from chloride solutions. Despite its importance to the development of thin film materials, the fundamentals of nucleation mechanisms governing the electrodeposition of iron have not been studied. For example,

\* Corresponding author. Tel.: +1 208 885 6569; fax: +1 208 885 2855.  
E-mail address: pesic@uidaho.edu (B. Pesic).

the extensive review article on the nucleation mechanism of various metals on various substrates by Hyde and Compton [16] has no mention of iron.

The objective of this work is to study the iron nucleation mechanisms during electrodeposition from two, sulfate and chloride, electrolytes. The morphological examination of the electrodeposited nuclei was performed by atomic force microscopy. Vitreous carbon was selected as the deposition substrate because of increased interest in carbon based materials by the electronic industry.

## 2. Experimental

Reagent grade  $\text{FeSO}_4 \cdot 7\text{H}_2\text{O}$  or  $\text{FeCl}_2 \cdot 4\text{H}_2\text{O}$  were used to prepare 0.001, 0.005, and 0.01 M  $\text{Fe}^{2+}$  sulfate or chloride solutions, respectively. Solutions (20 ml), prepared with deionized water (Type I purity water, Barnstead Nanopure II, 18.2 M $\Omega$ ), were deaerated in the electrochemical cell by purging argon gas for 10 min prior to electrochemical experimentation. All sulfate solutions contained 0.5 M reagent grade  $\text{Na}_2\text{SO}_4$ , while all chloride solutions contained 0.5 M NaCl, as supporting electrolytes.

The electrochemical setup was a standard three-electrode cell with vitreous carbon ( $0.442 \text{ cm}^2$ ; a non-porous disk-Sigri) as a working electrode, platinum foil as a counter electrode, and a silver–silver chloride reference electrode (Cypress Systems microelectrode,  $E_h^0 = +0.222 \text{ V}$ ). The working electrode was prepared by polishing with successively finer grades of abrasive paper, followed by wet polishing with 1 and  $0.05 \mu\text{m}$  alumina on a wet polishing cloth. The final step was polishing with dry  $0.05 \mu\text{m}$  alumina on a coarsely sanded glass plate. The electrode was then sonicated briefly in deionized water to dislodge remaining alumina particles, and then dried in a stream of nitrogen gas. This method of preparation provides the surface that is both electrochemically reproducible (tested by measuring the peak separation of ferrous/ferric cyanide redox couple), and smooth (roughness close to  $1 \text{ nm rms}$ —root mean square), which is of importance for the nucleation studies. The electrochemical experiments were executed by a potentiostat/galvanostat (Ametek, PAR 273A) controlled by a PC running the electrochemical software (PAR, M270).

Surface morphology, cross-sectional and population density analysis, of iron deposits were characterized by atomic force microscopy (VEECO, Digital Instruments, Model Nanoscope IIIa-MultiMode, tapping mode in fluid).

## 3. Results and discussion

### 3.1. Cyclic voltammetry

In order to determine the characteristic potentials in the two investigated iron systems, such as deposition potential,

the onset of hydrogen reduction reaction, and the onset of anodic oxidation, a set of cyclic voltammetry experiments was performed in both systems. All cv experiments were initiated at the open circuit potential (ocp) in a negative direction, reversed at  $-1300 \text{ mV}$  in a positive direction, then again reversed in a negative direction at  $+400 \text{ mV}$ . The initial ocp was the terminal potential.

Iron speciation in solutions was examined by constructing the  $E_h$ –pH, and distribution pH diagrams (not presented herein) for all investigated solution compositions by using the Win-Stabcal computer program [17]. In the sulfate systems, iron is predominantly present as free  $\text{Fe}^{2+}$  ions, while in the chloride systems ferrous ions are complexed into  $\text{FeCl}^+$ . However, because Drazic [18] has shown that iron hydroxide formation is possible on the surface of iron even at low pH, the participation of iron hydroxide species in iron electrodeposition was also considered.

Although the ionic strength of background electrolytes, 0.5 M  $\text{Na}_2\text{SO}_4$  and 0.5 M NaCl, was different, their activities were relatively close [19], 0.255 and 0.335, respectively, as verified by the negligible difference of the Nernst  $\text{Fe}^{2+}/\text{Fe}^0$  redox potentials (only 3.5 mV) in these two electrolytes.

#### 3.1.1. Hydrogen reduction on vitreous carbon

The surface of vitreous carbon electrode is known to inhibit hydrogen reduction even at highly negative potentials [20], whereas a metal surface in the same potential region can serve as catalytic site for hydrogen reduction. In order to distinguish the hydrogen reduction on vitreous carbon from the hydrogen reduction on iron nuclei, a set of control experiments without the initially present ferrous iron were performed (Fig. 1).

According to Fig. 1a and b, at pH 2, the onset of hydrogen reduction is at  $-850$  and  $-900 \text{ mV}$ , in the sulfate and chloride solutions, respectively. There was no hydrogen evolution at pH 5, in either solution.

Fig. 1a and b shows that concurrent reduction of iron and hydrogen on vitreous carbon surface will take place only in pH 2 solutions at potentials more negative than the indicated potentials ( $-850 \text{ mV}$  for sulfate and  $-900 \text{ mV}$  for chloride solutions).

#### 3.1.2. Sulfate system

Fig. 1a and b shows the effect of scanning rate on cv at pH 2 and 5, respectively. The initial ocp at pH 2 was  $+150 \text{ mV}$ , while at pH 5 this value was  $-70 \text{ mV}$ . The position of the first cathodic peak  $I_c$  was pH dependent. Thus, at pH 2, the peak  $I_c$  formed at about  $-1200 \text{ mV}$ , while at pH 5 it was between  $-1000$  and  $-1100 \text{ mV}$  (Fig. 2).

Peak  $I_c$ , which corresponds to iron deposition, was of much higher magnitude in pH 2 than in pH 5 solutions, for all three scanning rates, the reason being the additional current from reduction of hydrogen ions (1):



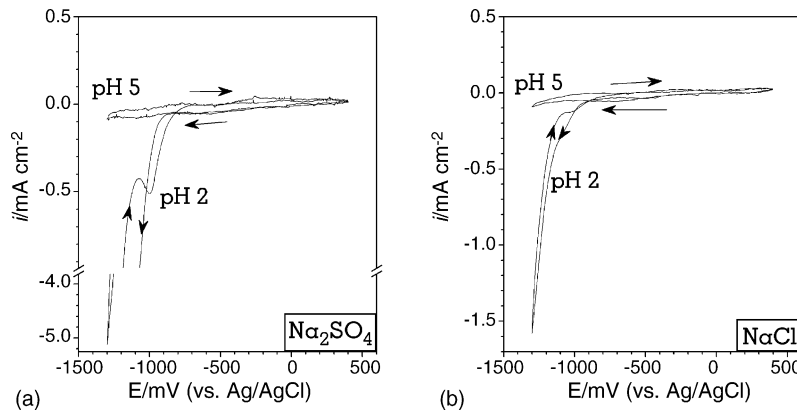


Fig. 1. Control cv's recorded in iron-free (a) sulfate and (b) chloride solutions at pH 2 and 5. The axis break between  $-0.9$  and  $-4 \text{ mA cm}^{-2}$  in (a) is introduced for clarity. Conditions:  $0.5 \text{ M Na}_2\text{SO}_4$ , or  $0.5 \text{ M NaCl}$ ; scanning rate  $20 \text{ mV s}^{-1}$ .

Hydrogen reduction in reaction (1), given in the most simplified form, is followed by an eventual release of hydrogen gas bubbles. Because control cv at pH 5 (Fig. 1a), was not characterized by a hydrogen reduction peak, an important conclusion is that the reduction of hydrogen ions occurs only on the formed iron nuclei. Evolution of hydrogen gas bubbles was readily observed visually, especially for pH 2 solutions.

Upon the sweep reversal in the anodic direction, the current became anodic at about  $-650 \text{ mV}$ , for pH 2 solutions. It then formed one anodic peak  $I_a$ , which corresponds to oxidation of deposited iron, and then diminished. At pH 5, the current became anodic at around  $-850 \text{ mV}$ , formed a small anodic peak, and then remained anodic until the next potential reversal at  $+400 \text{ mV}$ , indicating incomplete anodic dissolution of deposited iron. The equilibrium redox  $\text{Fe}^{2+}/\text{Fe}^0$  potentials, determined from the half-peak potentials of  $I_c$  and  $I_a$ , were  $-890 \text{ mV}$  at pH 2 and  $-850 \text{ mV}$  at pH 5.

The shape of anodic peaks at pH 2 and 5 indicates different iron speciation during electrodissolution. At pH 2, the well-defined anodic peak and the absence of a subsequent anodic current indicates straightforward formation of uncomplexed ferrous ions. On the other hand, the wavy and ill-defined anodic peaks at pH 5 most likely appear due to formation of the passive iron hydroxide film, implying that reduction–oxidation pathway of iron involves formation of

hydroxide species [18]. Mechanisms behind the anodic peaks will not be discussed any further since these are out of scope of the present study. A reader should consult a significant body of literature on the given subject elsewhere, for example in Refs. [18,21].

Electrodeposition of iron was also verified by the AFM study of the electrode surface at the characteristic crossover potentials (Fig. 3a–d). For each cv, the electrode was imaged at the potential, at which the current trace in the positive direction crosses over the current trace in the negative direction [22].

From Fig. 3a–d, it is apparent that the lower solution pH results in the higher nuclei population density, a phenomenon that will be further elaborated in the chronoamperometry section. The absence of deposited metallic iron at pH 2 and  $50 \text{ mV s}^{-1}$ , due to more negative onset of iron deposition potential, correlates well with the absence of peak  $I_a$  in the corresponding cv.

### 3.1.3. Chloride system

Fig. 4a and b presents the cycling voltammograms in chloride systems.

In these systems, the initial ocp was  $+230$  and  $-10 \text{ mV}$ , at pH 2 and 5, respectively. Only one cathodic peak,  $I_c$ , representing the reduction of ferrous iron to metallic form, was present at both pH 2 and 5. Compared to the sulfate system,

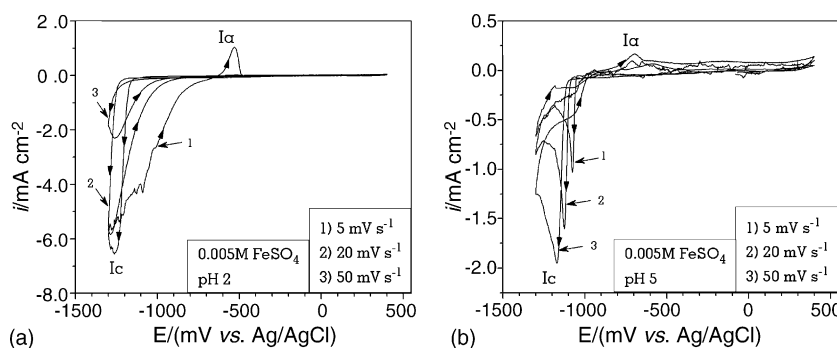


Fig. 2. Cyclic voltammograms of iron in sulfate system as a function of scanning rate at (a) pH 2 and (b) pH 5. Conditions:  $0.005 \text{ M Fe}^{2+}$ ,  $0.5 \text{ M Na}_2\text{SO}_4$ .

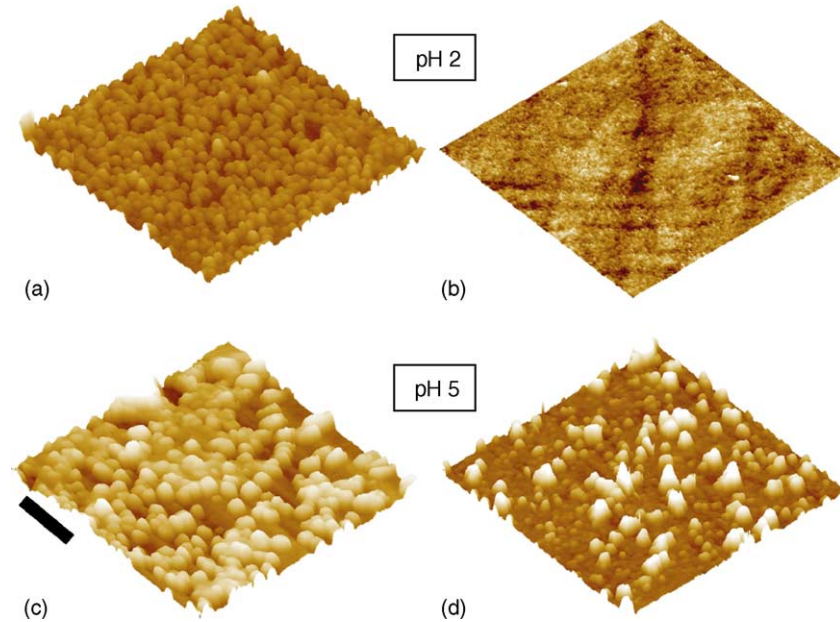


Fig. 3. Electrode surface at the crossover potential at pH 2: 5 and  $50 \text{ mV s}^{-1}$ , (a) and (b), respectively, and pH 5: 5 and  $50 \text{ mV s}^{-1}$ , (c) and (d), respectively. Conditions:  $0.005 \text{ M Fe}^{2+}$ ,  $0.5 \text{ M Na}_2\text{SO}_4$ ; scale bar:  $500 \text{ nm}$ , image heights:  $200 \text{ nm}$ .

peak  $I_c$  at pH 2 (Fig. 3a) was less obscured by hydrogen reduction current because the hydrogen ion reduction reaction was shifted in a more negative direction. Consequently, at pH 2, the cathodic currents at the vertex potential ( $-1300 \text{ mV}$ ) were lower in the chloride systems. Upon the sweep reversal at  $-1300 \text{ mV}$  the current became anodic at  $-625 \text{ mV}$  and formed a single anodic peak  $I_a$ , representing the oxidation of deposited iron.

At pH 5 (Fig. 4b), cathodic current traces were similar to the current traces in the sulfate system. The hydrogen ion reduction reaction started close to the vertex potential ( $-1300 \text{ mV}$ ), as indicated by the second increase of cathodic current towards the negative limit of the cv scans. Upon the sweep reversal, the current became anodic at  $-880 \text{ mV}$ , formed the first anodic peak  $I_a$ , and then one or two additional anodic peaks, collectively labeled as  $IIa$ . The number of anodic peaks at pH 5 depended on the scanning rate. Again, no further attention was paid to the anodic branch of the reactions.

The morphology of iron deposited from chloride solutions was similar to the morphology of iron from sulfate solutions, and for that reason not presented here. The only difference was that the nuclei from chloride solutions were larger, and with sharper defined contours.

### 3.2. Chronoamperometry

When the potential is stepped from open circuit to a potential at which reduction of ferrous ions proceeds under diffusion control, the initially formed iron nuclei define the diffusion zones controlling further supply of ferrous ions. If the nuclei growth results in an overlap of these zones a chronoamperometric peak, characteristic for nucleation, is produced. The current beyond the peak becomes limited by the mass transfer of ferrous ions to the electrode surface, as described by the Cottrell equation [22]. Within the diffusion zone, the growth of already established iron nuclei can continue, or new nuclei can initiate on other nucleation sites. Current recorded

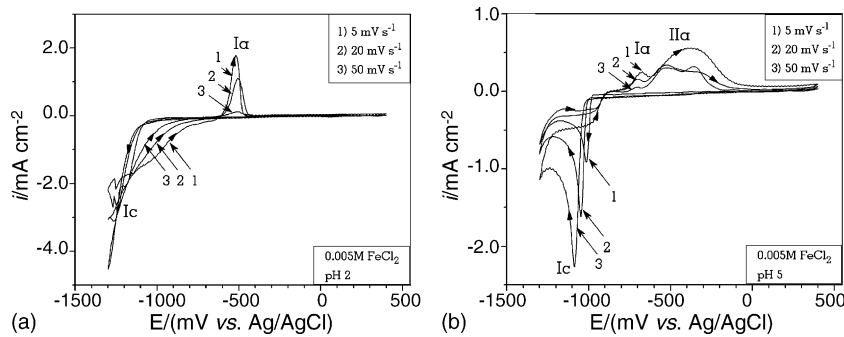


Fig. 4. Cyclic voltammograms of iron in chloride system as a function of scanning rate at (a) pH 2 and (b) pH 5. Conditions:  $0.005 \text{ M Fe}^{2+}$ ,  $0.5 \text{ M NaCl}$ .

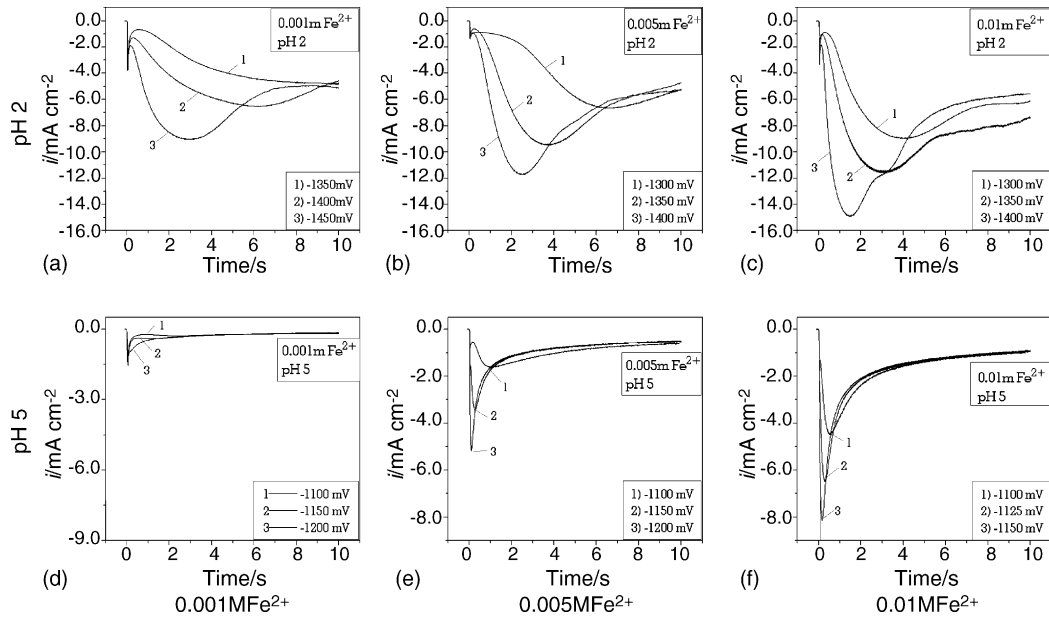


Fig. 5. Chronoamperograms of iron nucleation from sulfate solutions as a function of pH,  $\text{Fe}^{2+}$  concentration, and deposition potential. All experiments performed with 0.5 M  $\text{Na}_2\text{SO}_4$  as a supporting electrolyte.

during the transition from a no-reaction state to a steady-reaction state serves as an indicator of the type of nucleation mechanisms.

The varied parameters of interest in chronoamperometric experiments in sulfate and chloride systems were deposition potential, concentration of ferrous ions, solution pH, and temperature.

### 3.2.1. The sulfate systems

The chronoamperometry of iron nucleation from sulfate systems was examined as a function of pH (pH 2 and 5), ferrous sulfate concentration (0.001, 0.005, and 0.01 M  $\text{Fe}^{2+}$ ) and deposition potential (Fig. 5a–f).

According to Fig. 5a–f, chronoamperograms are strongly affected by the solution pH. The most notable difference is that the chronoamperograms at pH 2, for all three ferrous ion concentrations, show: (1) broader and shifted to longer times peaks, (2) that the mass-transfer limited current decayed more slowly and could not be fitted by the Cottrell equation, and (3) the later stages of ca became wavy for higher iron concentrations. The above-listed features of chronoamperograms at pH 2 are characteristic for a deposition process accompanied by a simultaneous hydrogen ion reduction. The shifting of peaks to longer times, compared to the peak positions at pH 5, is indicative of the prolonged time required for the localized diffusion zones to overlap, possibly due to the interference by the surface adsorbed hydrogen bubbles.

According to the earlier discussion of cyclic voltammograms in Fig. 1a, at pH 2, hydrogen ion reduction takes place on iron nuclei simultaneously with iron deposition. Association of molecules of reduced hydrogen into bubbles and their screening of the electrode surface results in the wavy appearance of the cas at the longer experimental times.

In order to estimate the contribution of the hydrogen ion reduction reaction, the peak current densities, chosen from equi-potential cas at pH 2 and 5, are plotted as a function of iron concentration, as shown in Fig. 6. Because the peak currents are directly proportional to the concentration of reacting species [23], it follows that the plot of peak current densities versus concentration should extrapolate to the origin if there are no parallel electrochemical reactions.

According to Fig. 6, the peak currents of cas could be extrapolated to zero for zero iron concentration only at pH 5, an indicator of the absence of hydrogen ion reduction in the initial stages of nucleation, which was not the case at pH 2. It should be noted that the analysis relevant to the data

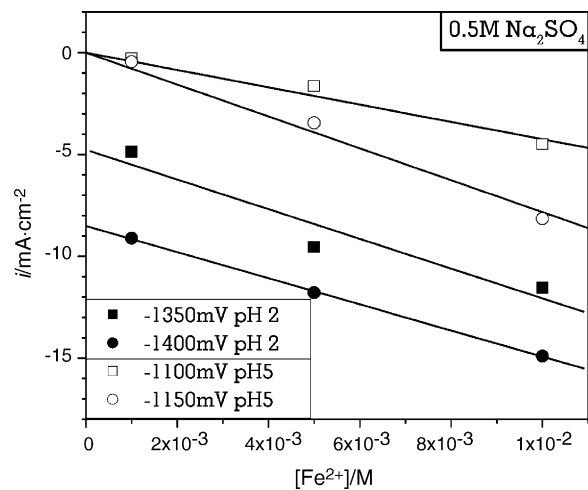


Fig. 6. Peak current density as a function of iron concentration. Data taken from cas in Fig. 5a–f for pH 2 (solid symbols) at: -1350 and -1400 mV, and for pH 5 (open symbols) at: -1100, and -1150 mV.

presented in Fig. 6 is only a qualitative confirmation of the accompanying cathodic reactions.

**3.2.1.1. Morphology.** The effect of iron concentration on the morphology of deposited iron nuclei is represented by the AFM images of the electrode surface after 10 s of iron deposition (Fig. 7a–f). Each of the AFM figures is accompanied by the corresponding nuclei height distribution histograms. The height measurements were chosen to represent the nuclei size (diameter) in order to avoid the tip-nucleus convolution. Further clarification to be made is that the number of nuclei used for size distribution determination is much larger (entire scanned area encountered) than the number of nuclei shown in the corresponding AFM images (typically a section cutout from the scanned area).

According to Fig. 7a–f, for all investigated concentrations, the nuclei deposited at pH 2 are of narrower size distribution, concentrated around smaller average nuclei size, than the nuclei at pH 5. Also, the increase of nuclei size with the increasing iron concentration was more pronounced at pH 5. Smaller nuclei sizes and narrower size distributions at pH 2 can be related to the evolution of hydrogen bubbles, most likely via electrode surface shielding effects causing

the localized variation of the free electrode surface and the consequent current density. At pH 5, due to the suppressing conditions for hydrogen evolution, the growth of iron nuclei is unhindered, resulting in a broader nuclei size distribution. So far, similar effect was observed only in the nucleation studies of ferromagnetic metals, cobalt [24] and nickel [25]. On the other hand, Jartych et al. [15] found no pH effect on the morphology of deposited iron; however, their study was performed in a very narrow range (pH 1.9–2.4).

The morphology of iron nuclei as a function of deposition potential is presented in Fig. 8a–f. Accordingly, the more cathodic deposition potential causes broader size distribution, especially at pH 5. However, the pH was a more effective parameter than the deposition potential, as the nuclei deposited from pH 2 solutions were of smaller size and narrower size distribution than the nuclei deposited at pH 5. The dominant role of pH can be explained by the above discussion on the shielding role of hydrogen bubbles.

### 3.2.2. The chloride system

As for the sulfate systems, the chronoamperometry of iron nucleation from chloride solutions was examined as a function of pH (pH 2 and 5), ferrous chloride concentration

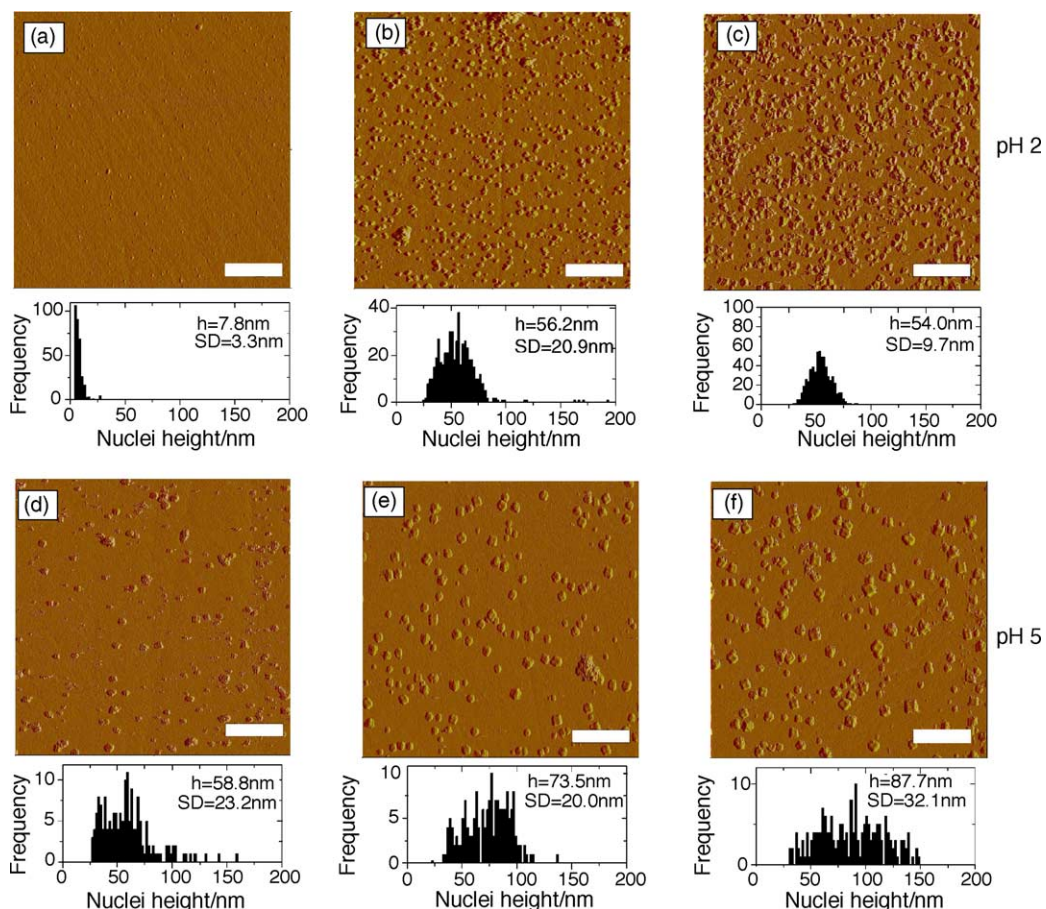


Fig. 7. Effect of iron sulfate concentration on nuclei morphology at pH 2 and 5. Each AFM image has a corresponding nuclei height distribution histogram ( $h$ : mean height; S.D.: standard deviation). Conditions: deposition time 10 s; deposition potentials:  $-1400\text{ mV}$  at pH 2 (a–c), and  $-1150\text{ mV}$  at pH 5 (d–f). Supporting electrolyte  $0.5\text{ M Na}_2\text{SO}_4$ ; scale bar  $1\text{ }\mu\text{m}$ .

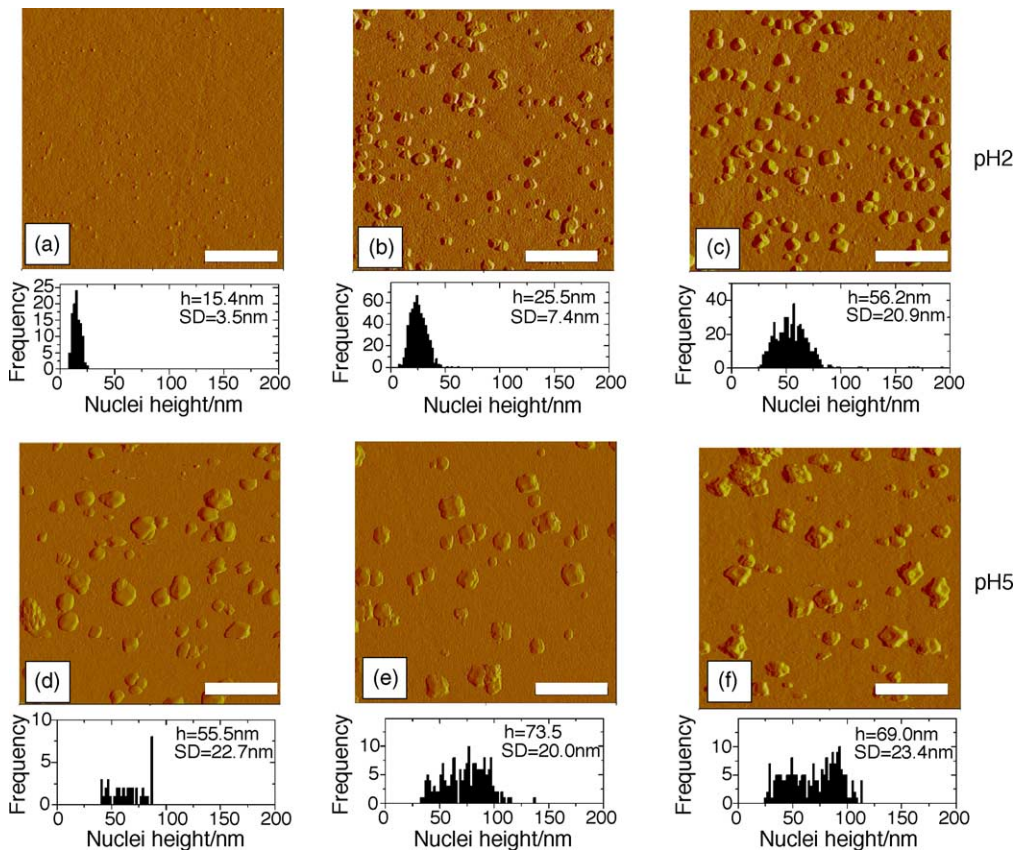


Fig. 8. Effect of deposition potential on morphology of iron nuclei deposited from solution at pH 2 (a–c) and pH 5 (d–f). Conditions: deposition potential (a) –1300 mV, (b) –1350 mV, (c) –1400 mV, (d) –1100 mV, (e) –1150 mV and (f) –1200 mV; 0.005 M FeSO<sub>4</sub>; supporting electrolyte 0.5 M Na<sub>2</sub>SO<sub>4</sub>; scale bar 500 nm.

(0.001, 0.005, and 0.01 M Fe<sup>2+</sup>) and deposition potential (Fig. 9a–f).

As a distinction from the sulfate systems, the effect of pH on cas is characterized by the presence of two current density peaks. The magnitude of the first peak depends only on deposition potential, while the second peak appears to be a function of the iron concentration, Fig. 9b and c. The observed independence of the first peak on the iron concentration might be masked by the current contribution from hydrogen ion reduction (fixed at fixed pH). As for the sulfate systems, the role of hydrogen ion reduction during electrodeposition of iron from chloride solutions was also confirmed from the peak current density vs. iron concentration plot (Fig. 10).

As expected, at pH 2 the linear fits had an intercept for zero iron concentration, indicating hydrogen reduction as a parallel reaction. At pH 5, the straight line fits with zero intercept indicated no hydrogen ion involvement.

In order to confirm that the first ca peak, in addition to hydrogen reduction, also includes the reduction of iron a separate ca experiment for 2.8 s (end of the first peak in Fig. 9c) was followed by AFM imaging of the electrode surface (Fig. 11).

In Fig. 11, the electrode surface coverage with iron nuclei confirms the existence of ferrous ion reduction reaction even before the onset of the second peak.

Chronoamperograms with two peaks can seldom be found in the literature. Two chronoamperometric deposition peaks were observed by Arbib et al. [26], who studied rhodium nucleation onto gold, and proposed that the first peak was the result of a monolayer formation prior to the bulk deposition of rhodium. With respect to iron, electrodeposition studies were limited in number, and the few found used galvanostatic methods of deposition to prepare continuous iron films [9,13–15]. Discrete iron nuclei in Fig. 11 clearly show that the first peak cannot be assigned to the monolayer formation. Instead, due to the absence of two peaks in cas for the iron sulfate system (Fig. 5a–f), it is highly suggestive that it is the presence of chloride ions that could be responsible for the two peaks in chloride solutions.

In order to examine the role of chloride ions, the concentration of the sodium sulfate supporting electrolyte was sequentially replaced by sodium chloride, so that the concentration of sodium sulfate decreased from 0.5 to 0 M, while the concentration of sodium chloride simultaneously increased from 0 to 0.5 M.

In the absence of chloride ions, the chronoamperogram in Fig. 12 shows only one broad peak (curve 1). Upon subsequent addition of chloride ions, the shape of the chronoamperograms begins to change: the peak current

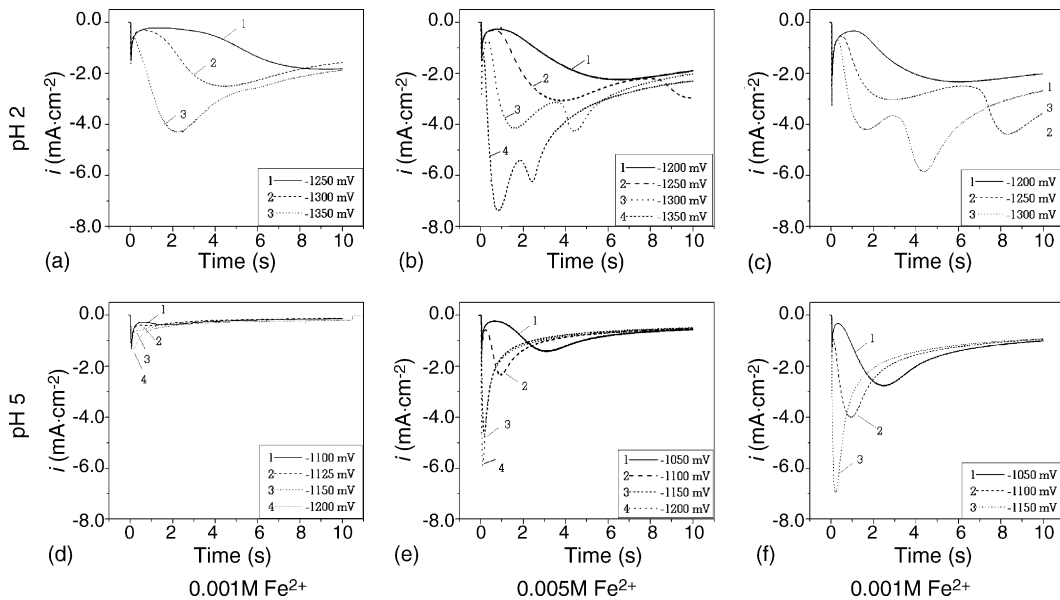


Fig. 9. Chronoamperograms of iron nucleation from chloride solutions as a function of pH,  $\text{Fe}^{2+}$  concentration, and deposition potential. The iron concentrations used were: 0.001 M  $\text{Fe}^{2+}$  (a and d); 0.005 M  $\text{Fe}^{2+}$  (b and e); 0.01 M  $\text{Fe}^{2+}$  (c and f). All experiments performed with 0.5 M NaCl as supporting electrolyte.

density becomes lower due to the suppressed hydrogen reduction, and an additional peak appears.

According to Fig. 9d–f, the presence of chloride ions at pH 5 was ineffective, as the cas resembled those from sulfate system at the corresponding pH.

**3.2.2.1. Morphology.** Morphological characterization of electrodeposited iron nuclei as a function of solution pH and iron concentration is presented in a series of AFM images in Fig. 13a–f.

Accordingly, the iron nuclei deposited from chloride solutions had somewhat broader height distribution, and slightly

larger average nuclei size, in comparison to the sulfate system.

The effect of deposition potential on the morphology of deposited iron nuclei is presented in Fig. 14a–f.

The effect deposition potential in chloride solutions is very similar to the described effect of deposition potential in sulfate solutions.

In general, there was very little difference between the sulfate and chloride systems, for the corresponding pH, with respect to the morphology (nuclei size and size distribution) of iron nuclei.

### 3.2.3. Current efficiency during iron electrodeposition

The contribution from hydrogen reduction has to be accounted for in the analysis of current transients in the electrodeposition studies, especially if a metal deposition

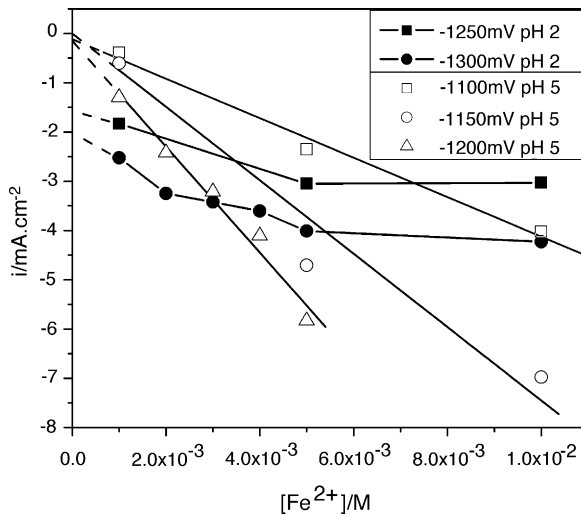


Fig. 10. Peak current density as a function of iron concentration. Data taken from cas in Fig. 9a–f for pH 2 (solid symbols) at:  $-1250$ ,  $-1300$ ,  $-1100$  mV, and for pH 5 (open symbols) at:  $-1150$ , and  $-1200$  mV.



Fig. 11. Electrode surface at the end of the first current density peak at pH 2. Conditions: 0.01 M  $\text{FeSO}_4$ ; 0.5 M  $\text{Na}_2\text{SO}_4$ ;  $E_{\text{dep}} = -1300$  mV;  $t_{\text{dep}} = 2.8$  s; scale bar 500 nm.

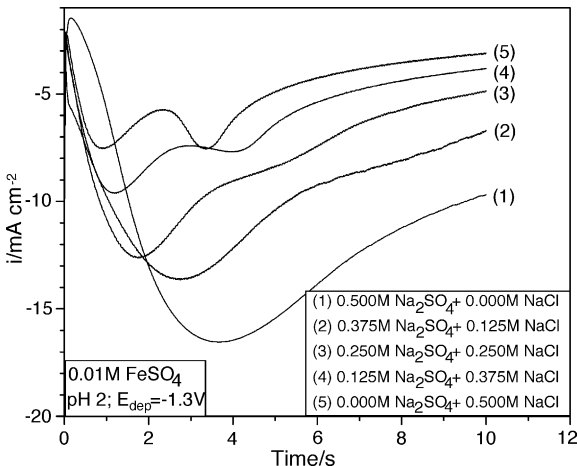


Fig. 12. Effect of chloride ion concentration on the number of peaks in chronoamperograms at pH 2. Conditions: 0.01 M  $\text{FeSO}_4$ ;  $E_{\text{dep}} = -1.3 \text{ V}$ ; pH adjusted by dilute  $\text{H}_2\text{SO}_4$ .

potential is more negative than that of hydrogen ion reduction. In this study, the current efficiency for iron deposition was estimated by a non-destructive AFM/chronoamperometry method, previously described in [24]. The method compares

the weight of iron calculated by using Faraday's law to the weight of iron calculated from the measured volume of iron in the AFM images. The current efficiency results are presented in Fig. 15.

According to Fig. 15, for pH 5 solutions there is a very good agreement between the amount of deposited iron determined from the integration of current transients and AFM images, also indicative of high current efficiency. The large discrepancy between the weight of iron determined by the AFM and calculated by the integration of current transients at pH 2, on the other hand, is caused by the large contribution from reduction of hydrogen ions. The discrepancy is particularly large in the sulfate systems, indicative of a very low current efficiency, estimated between 1% and 13%. In the chloride systems, the estimated current efficiency is between 40% and 45%. The current efficiency analysis supports the discussion on the role of hydrogen ions in the cyclic voltammetry studies, presented above.

The above current efficiency is drastically different from those in industrial iron electroplating operations [1]. The discrepancy is explained via several important distinctions, such as the substrate, the electrodeposition voltage and the extent of electrodeposition. Industrial conditions use iron, or other

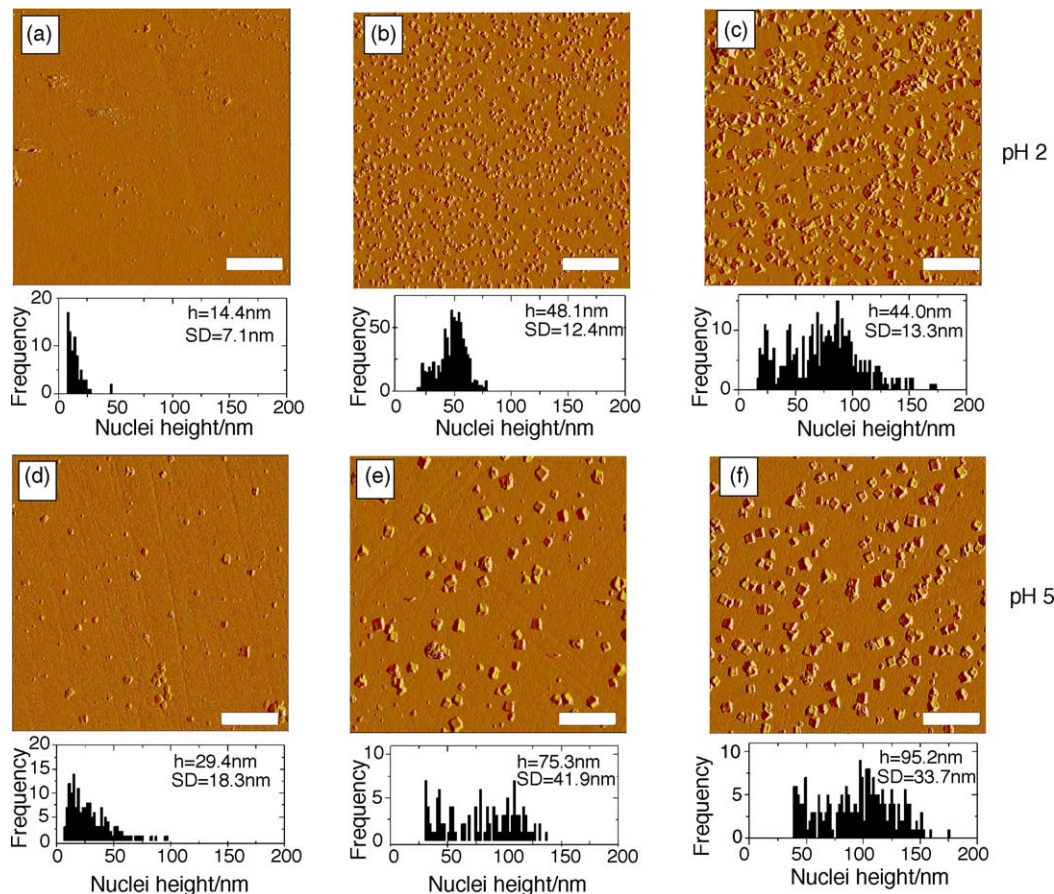


Fig. 13. Effect of iron chloride concentration on nuclei morphology at pH 2 and 5. Each AFM image has a corresponding nuclei height distribution histogram ( $h$ : mean height; S.D.: standard deviation). Conditions: deposition time 10 s; deposition potentials:  $-1300 \text{ mV}$  at pH 2 (a–c), and  $-1150 \text{ mV}$  at pH 5 (d–f); supporting electrolyte 0.5 M NaCl; scale bar 1  $\mu\text{m}$ .

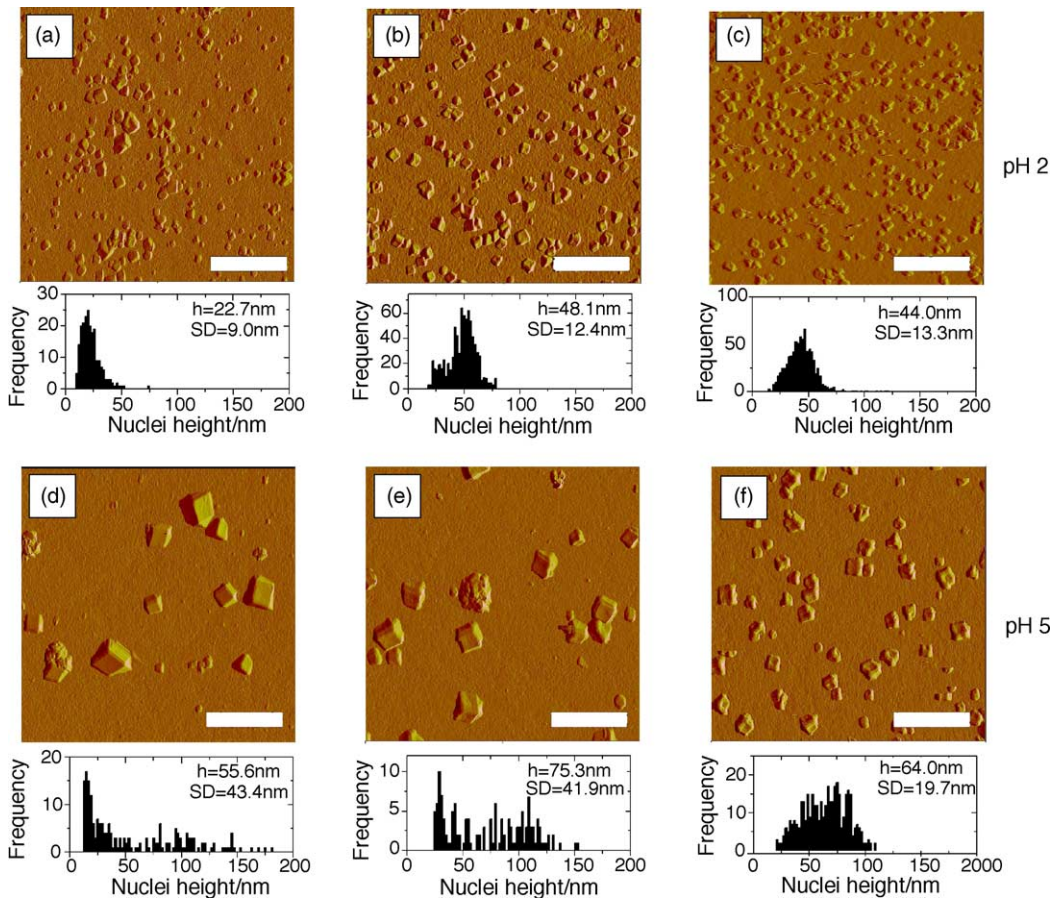


Fig. 14. Effect of deposition potential on morphology of iron nuclei deposited from chloride solution at pH 2 (a–c) and pH 5 (d–f). Conditions: deposition potential (a) –1250 mV, (b) –1300 mV, (c) –1350 mV, (d) –1100 mV, (e) –1150 mV, and (f) –1200 mV; 0.005 M FeSO<sub>4</sub>; supporting electrolyte 0.5 M NaCl; scale bar 500 nm.

metallic substrate for electrodeposition, which invariably result in much lower overvoltage requirements compared to the electrodeposition on vitreous carbon. Furthermore, the amount of current required for the nucleation stage is

negligible compared to the amount of current required for the electrodeposition of micrometer, or millimeter, thick films, and as such not distinguished from the overall current efficiency.

### 3.2.4. Effect of temperature

The morphology of iron deposits is strongly affected by the solution temperature [1,9,15]. The effect of temperature on the size and population density of electrodeposited nuclei was investigated in the solution temperature range 5–55 °C, in both sulfate and chloride systems (Fig. 16).

In the sulfate solutions, the population density of iron nuclei increases with the increase in solution temperature, moderately in the 5–45 °C temperature range, and then more rapidly between 45 and 55 °C.

In chloride solutions, the population density shows a non-linear, somewhat downward trend with temperature, with a minimum at 25 °C. The initial decrease of nuclei population density going from 5 to 25 °C could be related to desorption of chloride ions, which would allow for the growth of already formed nuclei, instead of the formation of new ones. The increase in nuclei population density from 25 to 55 °C is probably the result of the contraction of the diffusion layer due to thermal agitation, and the possible thermal activation

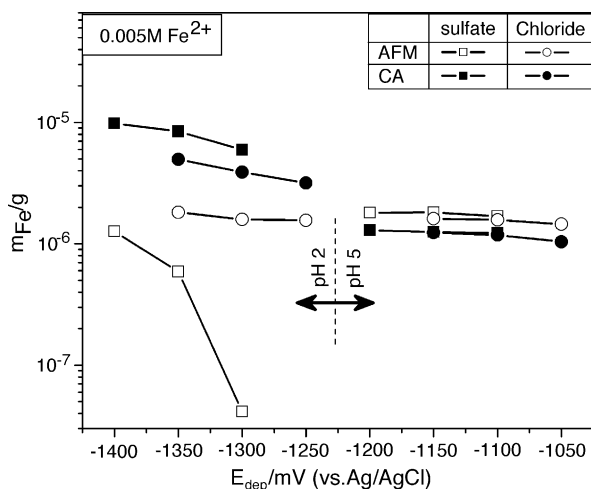


Fig. 15. Weight of iron deposited from sulfate and chloride solutions at pH 2 and 5, determined by integration of current transients and by AFM image analysis. Conditions: iron concentration 0.005 M Fe<sup>2+</sup>; supporting electrolyte 0.5 M Na<sub>2</sub>SO<sub>4</sub> or 0.5 M NaCl; deposition time 10 s.

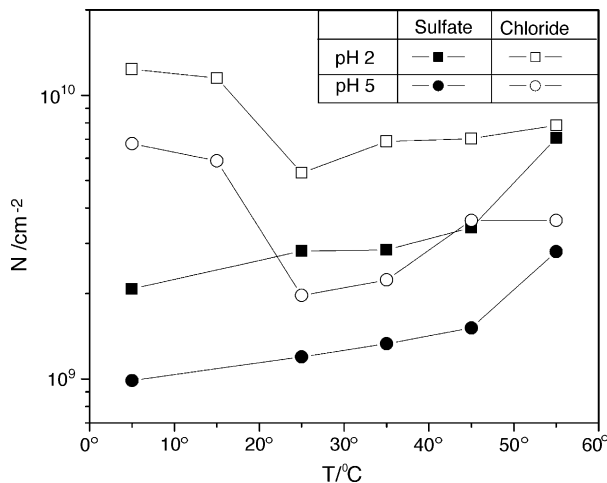


Fig. 16. Effect of electrolyte temperature on nuclei population density of iron deposited from sulfate and chloride solutions. Conditions: 0.005 M  $\text{FeSO}_4$  and 0.5 M  $\text{Na}_2\text{SO}_4$ ; or 0.005 M  $\text{FeCl}_3$  and 0.5 M  $\text{NaCl}$ ; deposition potential:  $-1350 \text{ mV}$  at pH 2;  $-1100 \text{ mV}$  at pH 5.

of nucleation sites, which could also explain the effect observed in the sulfate system.

The proposed mechanisms describing the unusual dependence of nuclei population density on temperature require further clarification. Although the effect of temperature on the morphology of iron deposits was investigated earlier [9,15], the studies were confined to the determination of crystallite sizes in continuous iron films, and are therefore not comparable to the results presented here.

### 3.2.5. Nucleation mechanisms

In order to determine the iron nucleation mechanisms, a model developed by Scharifker and Hills [23] was applied

to the chronoamperometric data presented in Sections 3.2.1 and 3.2.2. Instantaneous nucleation corresponds to a slow growth of nuclei on a small number of active sites, all activated in the same time. Progressive nucleation corresponds to fast growth of nuclei on many active sites, all activated during the course of electroreduction [27]. In order to distinguish between the two mechanisms, chronoamperometric data are plotted in reduced time-reduced current coordinates and compared to the expressions for instantaneous and progressive nucleation, Eqs. (2) and (3), respectively:

$$\frac{i^2}{i_m^2} = \frac{1.9542}{\frac{t}{t_m}} \left\{ 1 - \exp \left[ -1.2564 \left( \frac{t}{t_m} \right) \right] \right\}^2 \quad (2)$$

$$\frac{i^2}{i_m^2} = \frac{1.2254}{\frac{t}{t_m}} \left\{ 1 - \exp \left[ -2.3367 \left( \frac{t}{t_m} \right)^2 \right] \right\}^2 \quad (3)$$

where  $i_m$  is the current and  $t_m$  is the time coordinate of a chronoamperometric peak.

Chronoamperograms for the sulfate systems in Fig. 5a–f are presented in Fig. 17a–f in reduced current-reduced time coordinates, from which the nucleation models can be determined by comparison to the theoretical equations (2) and (3).

At pH 2, Fig. 17a–c, the iron nucleation mechanisms follow the progressive model from the initiation of an experiment until the peak was just past on the chronoamperograms,  $t/t_{\max} = 1.5$ . When  $t/t_{\max}$  is greater than 1.5, the reduced chronoamperograms start to deviate from the progressive nucleation model, most likely due to the contribution from the hydrogen reduction reaction. Iron nuclei deposited from pH 5 solutions (Fig. 17d–f), also follow the progressive nucleation mechanisms, but because of the absence of an interfering hydrogen reduction reaction, the reduced model

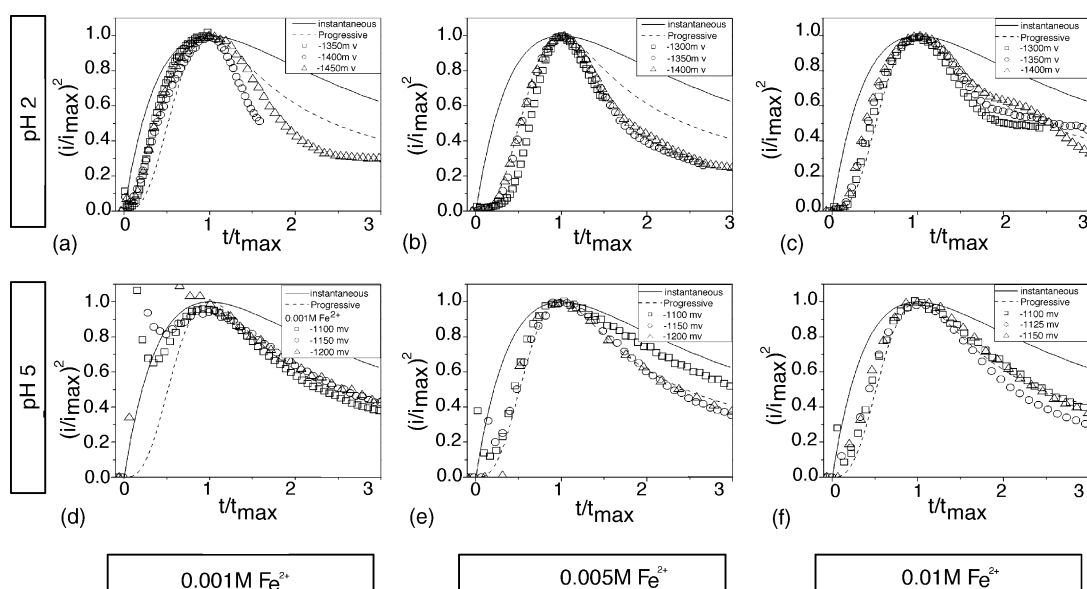


Fig. 17. Reduced current-reduced time plots of chronoamperograms in Fig. 5a–f as a function of iron concentration, solution pH, and deposition potential in sulfate systems. Solid line: instantaneous nucleation model and dashed line: progressive nucleation model. Conditions: 0.5 M  $\text{Na}_2\text{SO}_4$  supporting electrolyte.

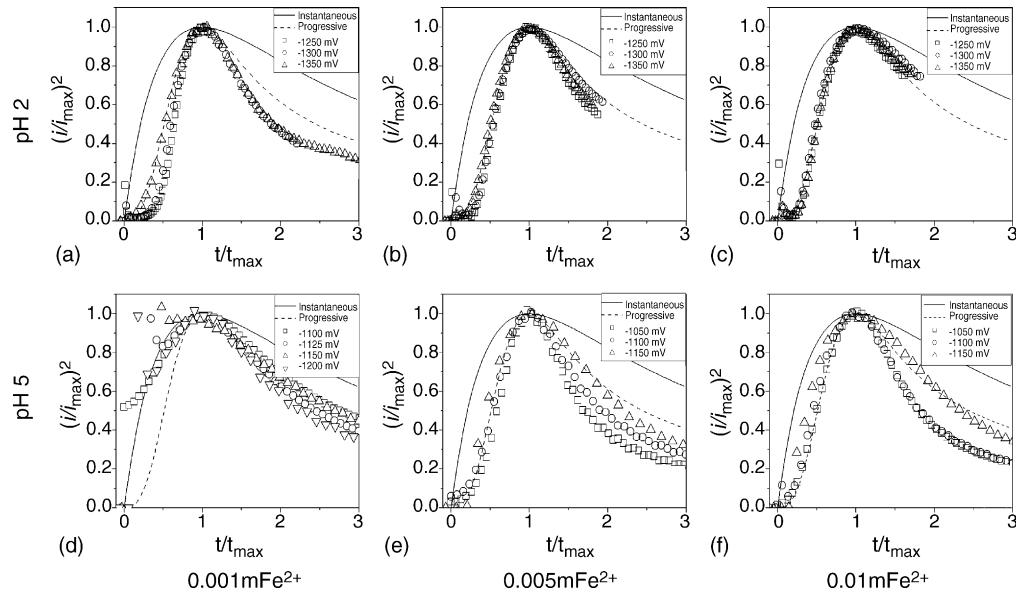


Fig. 18. Reduced current–reduced time plots of chronoamperograms from Fig. 9a–f as a function of iron concentration, solution pH, and deposition potential in chloride systems. Solid line: instantaneous nucleation model and dashed line: progressive nucleation model. Conditions: 0.5M NaCl supporting electrolyte.

chronoamperograms fit the theoretical curve for progressive nucleation in the entire investigated range.

For chloride systems, the reduced current–time chronoamperograms are presented in Fig. 18a–f.

At pH 2, as the raw chronoamperograms had two peaks, only the data corresponding to the first peak were used for fitting, and for higher iron concentrations (Fig. 18a–c). Iron nucleation followed progressive nucleation behavior. At pH 5, the reduced chronoamperograms also followed the progressive nucleation line, but deviated after passing the peak. Since the hydrogen reduction reaction can be ruled out as a possible cause for deviation, other explanations have to be sought. For example, Scharifker–Hills nucleation models were developed for the hemispherical type of nuclei, but this study has found that the geometry of iron nuclei is cubic. Further, inactivation of nuclei surface by adsorbed chloride species (iron-hydroxy-chloride) could be another possible reason for the negative deviation from the proposed theoretical models. It was also observed that some chronoamperograms (0.001 M Fe<sup>2+</sup>, pH 5) have high charging currents in the initial stages of iron nucleation, which can persist up to the nucleation peak and cause severe distortion of the initial segments of chronoamperograms. The observed charging currents are a consequence of charge accumulation in the double layer, as polished vitreous carbon electrodes are known to have high capacitance, increasing with the increasing of pH [28], in aqueous solutions.

### 3.2.6. Nucleation rate

According to the above theoretical models, the iron nucleation mechanisms follow the progressive nucleation model in both sulfate and chloride systems. One of the parameters characteristic for the progressive nucleation is the rate of appearance of new nuclei, which depends on the degree of

inhibition of nucleation sites. Because the population density is a function of the rate of appearance of new nuclei, which in turn is a function of the nucleation overpotential,  $\eta$ , as  $N \propto \eta^{-2}$  [29], it follows that the existence of inhibition mechanisms can be tested by measuring the nuclei population

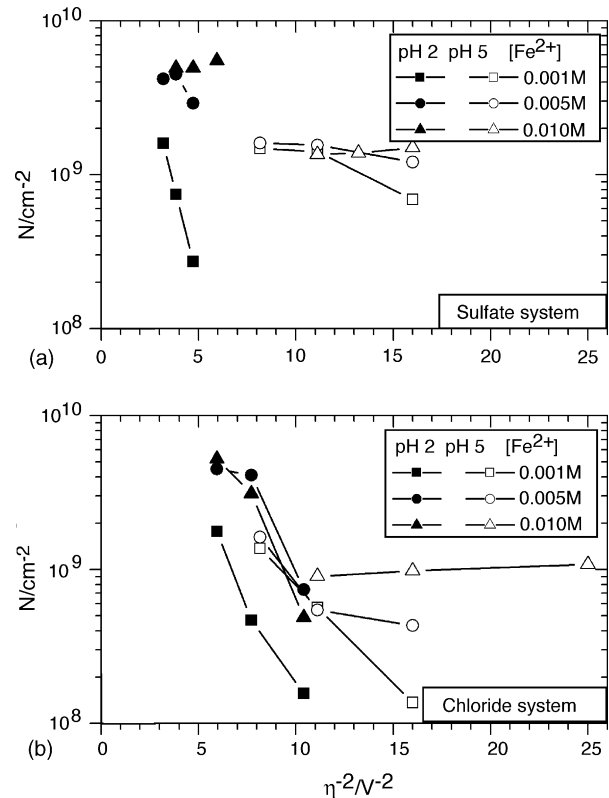


Fig. 19. Nuclei population densities as a function of nucleation overvoltage for (a) sulfate and (b) chloride solutions at pH 2 and 5.

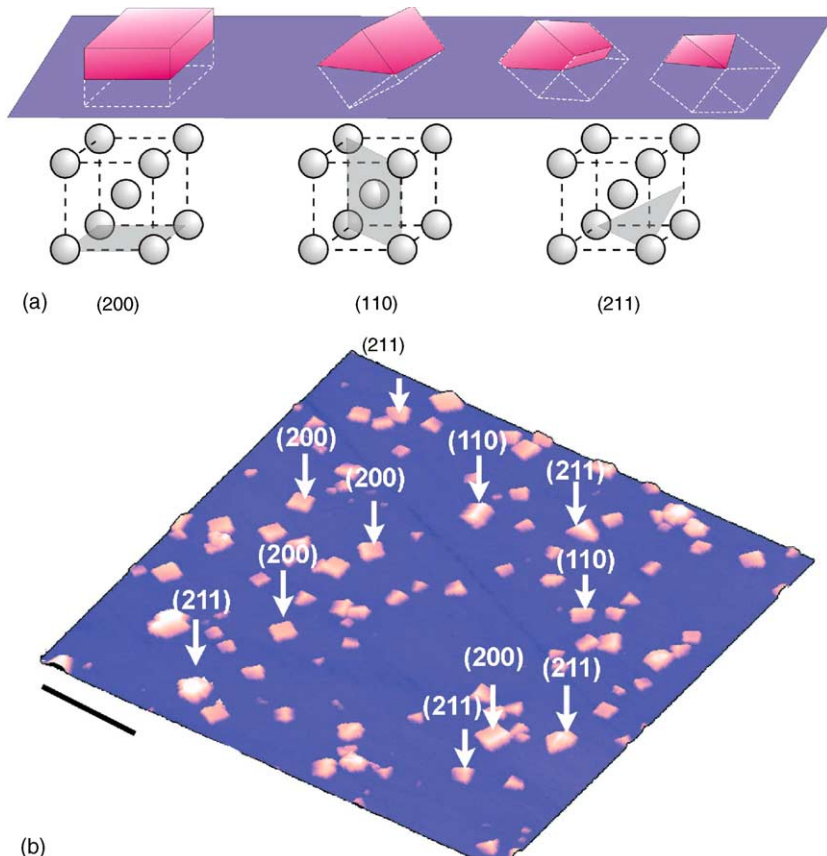


Fig. 20. (a) Schematic representation of three observed types of deposited iron nuclei, correlated to the crystallographic orientation of their (2 0 0), (1 1 0), and (2 1 1) basal planes in bcc iron lattice, and (b) 5  $\mu\text{m}$   $\times$  5  $\mu\text{m}$  AFM image of iron nuclei electrodeposited from the chloride system exhibiting the suggested crystallographic orientations. Conditions: 0.005 M  $\text{Fe}^{2+}$ , 0.5 M NaCl, solution pH 5; deposition at  $-1150\text{ mV}$  for 10 s; vertical scale 2500 nm; scale bar 1  $\mu\text{m}$ .

density as a function of overpotential, as given in Fig. 19a and b.

According to Fig. 19a, the nuclei population density in the sulfate system is overvoltage dependent only for deposition from 0.001 M  $\text{Fe}^{2+}$  solution at pH 2. In the chloride system, the dependency extends to all studied iron concentrations at pH 2, and 0.001 and 0.005 M  $\text{Fe}^{2+}$  solutions at pH 5. The non-zero slopes indicate inhibited nucleation, caused by the screening of active nucleation sites effects, either by already established diffusion zones, or by the hydrogen bubbles adsorbed on the surface.

### 3.3. Crystallography of electrodeposited iron, determined by AFM

Because of the small amounts of iron deposited in chronoamperometric experiments and a strong background signal of vitreous carbon, X-ray diffraction analysis of deposited iron was not possible. The growth of thicker iron films was not considered as an alternative because after secondary nucleation of iron on iron and further grain growth, the information on the initial crystallography of iron nuclei would be lost. The solution was found in resorting to the analysis of atomic force microscopy images in order to determine the possible crystallographic orientations of electrodeposited

iron on vitreous carbon. Iron nuclei in all of the AFM images appear to be well defined and with sharp edges, which is indicative of their single crystalline nature. This in turn enables the determination of their crystallography by AFM. The average size of iron nuclei at the end of the chronoamperometric experiments was between one hundred and several hundred nanometers, and the most prominent difference between iron nuclei deposited from chloride and sulfate solutions is that the cubic nature of iron was strongly expressed in the chloride system. All nuclei deposited from chloride solutions at both pH 2 and 5 were characterized by a distinct cubic shape, stemming from the body centered cubic lattice of iron. The body centered cubic (bcc) crystals of iron were found with three different orientations with respect to the substrate surface. Close examination of the AFM images of iron deposited from the sulfate system also reveals three types of nuclei, but with slightly tapered edges, which may indicate the appearance of crystallographic planes with higher symmetries.

The three types of observed iron nuclei, as well as their basal planes in relation to the bcc lattice of iron, are presented schematically in Fig. 20a. The top row schematically outlines the simulated 3D appearance of each of the three types of nuclei in the AFM image, with respect to the orientation of the primitive cube. Note that the nuclei growing with the (2 1 1) basal plane can appear in two forms, depending on

the extent of their growth, as indicated in the schematics in Fig. 20a. The related representative AFM image, containing iron nuclei with all three observed crystallographic symmetries, is presented in Fig. 20b. Crystallographic indices of the basal planes of several nuclei, denoted with arrows, are given, based on the AFM profiling analysis. Other, non-marked nuclei in the image can also be categorized into one of the three symmetries.

Calculations undertaken by Pangarov and Vitkova [30] predicted these three crystallographic orientations of iron as the most thermodynamically stable. While trigonal iron pyramids observed by Heusler and Knoedler [8] correspond to the nuclei with (2 1 1) basal plane, the tetragonal pyramids found in their study are absent here.

#### 4. Conclusions

Nucleation mechanisms of iron on vitreous carbon electrode have been investigated comparatively from sulfate and chloride solutions by the electrochemical techniques of cyclic voltammetry and chronoamperometry, supported by the morphological AFM studies. The following was found:

According to the cyclovoltammetric studies, the onset of iron deposition was less negative in chloride solutions than in sulfate solutions, and more negative at pH 2 than at pH 5. As confirmed by the control cv's, the extent of the hydrogen reduction reaction was larger at pH 2 than at pH 5 in both systems. Hydrogen evolution, prevalent in the sulfate system, was responsible for the low current efficiency observed. At pH 5, deposition possibly proceeds through the formation of iron hydroxide, or iron-hydroxy-chloride.

According to the theoretical models, iron nucleation is governed by the progressive nucleation mechanisms in both, sulfate and chloride, systems for each solution pH studied.

The AFM analysis revealed the presence of discrete three-dimensional iron nuclei of the following crystallographic orientations: (1 1 0), (2 0 0), and (2 1 1).

For both, pH 2 and pH 5, the nuclei population density increased with the increase of temperature in the sulfate systems, and initially decreased (minimum at 25 °C) then increased with the increase of temperature for the chloride systems.

Iron concentration increase generally had a positive effect on both the nuclei size and the population density in both systems.

The nucleation was less inhibited in the chloride systems.

#### Acknowledgements

This work was sponsored by the U.S. Department of Defense, Department of the Navy, Office of Naval Research,

Grant No. N000140110829, and The National Science Foundation RII Award (EPS 0132626).

#### References

- [1] M. Schlesinger, M. Paunovic, *Modern Electroplating*, 4th ed., Wiley, New York, NY, 2000, pp. ix and 461.
- [2] E.M. Levy, *Plating* 56 (1969) 903.
- [3] H.V. Venkatasetty, *J. Electrochem. Soc.* 117 (1970) 403.
- [4] M. Sarojamma, T.L. Rama Char, *Met. Finish.* 70 (9) (1972) 36.
- [5] S. Gowri, B.a. Shenoi, *Met. Finish.* 70 (6) (1972) 30.
- [6] H.E. Austen, *J. Electrochem. Soc.* 117 (1970) 403.
- [7] K.V. Gow, G.J. Hutton, *Electrochim. Acta* 17 (1972) 1797.
- [8] K.E. Heusler, R. Knoedler, *Electrochim. Acta* 15 (1970) 243.
- [9] S. Yoshimura, S. Yoshihara, T. Shirakashim, E. Sato, *Electrochim. Acta* 39 (4) (1994) 589.
- [10] W. Schindler, O. Schneider, J. Kirschner, *J. Appl. Phys.* 81 (8) (1997) 3915.
- [11] E.A. Abd El Meguid, S.S. Abd El Rehim, E.M. Moustafa, *Thin Solid Films* 443 (2003) 53.
- [12] K.-M. Yin, B.-T. Lin, *Surf. Coat. Technol.* 78 (1996) 205.
- [13] E. Jartych, D. Chocyk, M. Budzynski, M. Jalochowski, *Appl. Surf. Sci.* 180 (2001) 246.
- [14] E. Jartych, J.K. Zurawicz, E. Maczka, J. Borc, *Mater. Chem. Phys.* 72 (2001) 356.
- [15] E. Jartych, M. Jalochowski, M. Budzynski, *Appl. Surf. Sci.* 193 (2002) 210.
- [16] M.E. Hyde, R.G. Compton, *J. Electronal. Chem.* 549 (2003) 1–12.
- [17] H.-H. Huang, STABCAL: stability calculation for aqueous systems, (2001 version), Montana Tech, The University of Montana, Butte, MT.
- [18] D.M. Drazic, in: B.E. Conway, J. O'M Bockris, R.E. White (Eds.), *Modern Aspects of Electrochemistry*, no. 19, Plenum Press, New York, NY, 1989, p. 69.
- [19] J.F. Zemaitis Jr., D.M. Clark, M. Rafal, N.C. Scrivner, *Handobook of Aqueous Electrolyte Thermodynamics*, AICE, New York, NY, 1986, pp. 111 and 122.
- [20] K. Kinoshita, *Carbon, Electrochemical and Physicochemcial Properties*, Wiley, New York, NY, 1988.
- [21] I.-H. Plonski, in: B.E. Conway, J. O'M Bockris, R.E. White (Eds.), *Modern Aspects of Electrochemistry*, no. 29, Plenum Press, New York, NY, 1995, p. 203.
- [22] T.J. Kemp (Ed.), *Southampton Electrochemistry Group Instrumental Methods in Electrochemistry*, Ellis Horwood Ltd., Chichester, UK, 1985.
- [23] B. Scharifker, G. Hills, *Electrochim. Acta* 28 (7) (1983) 879.
- [24] D. Grujicic, B. Pesic, *Electrochim. Acta* 49 (2004) 4719.
- [25] M.P. Zach, R.M. Penner, *Adv. Mater.* 12 (12) (2000) 878.
- [26] M. Arbib, B. Zhang, V. Lazarov, D. Stoychev, A. Milchev, C. Buess-Herman, *J. Electronal. Chem.* 510 (2001) 67.
- [27] M.P. Pardave, M.T. Ramirez, I. Gonzales, A. Serruya, B.R. Scharifker, *J. Electrochem. Soc.* 143 (5) (1996) 1551.
- [28] A. Dekanski, J. Stevanovic, R. Stevanovic, B.Z. Nikolic, V.M. Jovanovic, *Carbon* 39 (2001) 1195.
- [29] A. Serruya, J. Mostany, B.R. Scharifker, *J. Electroanal. Chem.* 446 (1999) 39.
- [30] N.A. Pangarov, S.D. Vitkova, *Electrochim. Acta* 11 (1966) 1719.